3. The Methods

3.1. Geostatistics

Geostatistical methods (e.g., Matheron, 1962; 1970; Journel, 1977; Deutsch and Journel, 1992) are applied to analyze the distribution of a variable in space (2D), or in space and time (3D). Variography is one of them, examining the correlation of variable values across space, i.e., the spatial change of the variable value in the resulting variogram. These variograms are approximated by mathematical models that form the base for interpolation techniques (e.g., kriging). This allows filling unknown spaces with probable values, but is only valid, if the analysed variable is continuous over space and several other conditions are met (e.g., Matheron, 1962; 1970; Journel, 1977; Deutsch and Journel, 1992).

This study analyses the distribution of strain in the Central Andes. The original deformation data (database compiled from literature, Appendix A) includes geographical coordinates of the study areas as well as the beginning and end of deformation in the respective areas. Only those references were included that precisely documented the geographical location of the study area and the samples used for dating, as well as the dating method. In the original format, the data plot as polygons of various sizes and shapes.

I initially reorganized the data into a grid of points covering the entire area. To each of these points information is assigned on beginning and end of deformation for the given geographical position, so that the duration of deformation at each point can be calculated. Additionally, I included shortening estimates derived from balanced cross sections (compilation from Oncken et al., 2006), to gain shortening rates for every data point with a spatial resolution of 40 km, and a temporal scale of 1 Ma steps. These lower cut-off values represent the upper boundary of the error of the data, meaning that the data are not solid below these values.

For both the deformation activity and shortening rates the variables are continuously distributed in space, as they will only have positive values or be zero. However, I could not use our variogram models for interpolation as we do not precisely know which of the natural boundaries (e.g., faults) have to be accounted for dividing the entire area into subareas. For the same reason, we did not use 3D models: it is hard to distinguish the limits of the correlation between points that are at a distance, spatially and temporally. Therefore, we only employ spatial 2D analysis for each time window of 1 Ma.

Variogram analysis requires that variables are given with geographical coordinates (x/y) and individual values. The variation in variable values from one point to another separated by a distance h (lag spacing) is calculated according to this formula (Fig. 3.1):

$$\gamma^*(h) = \frac{1}{2\,N(h)} \sum_{i=1}^{N(h)} \left[z(x_i) - z(x_i + h) \right]^2$$

Fig. 3.1: Formula for semi-variogram

This is done for every distance h and in all possible directions (Fig. 3.2).

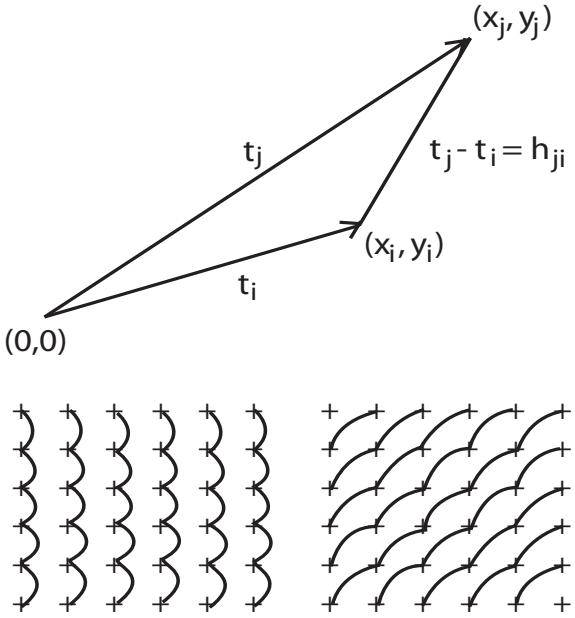

Fig. 3.2: Graphical representation of the distance h between points. "h" is calculated for all possible directions.

All distances h are plotted on the x-axis against the variation (y-axis).

The omnivariogram includes all directions at once, whereas directional variograms can be calculated for a given direction, which is necessary when the data show anisotropies, i.e., pronounced differences in some directions. Directions are given in degrees: East is 0, North is 90, West is 180 etc., counting counterclockwise. Such anisotropies can be easily detected on variogram surfaces, which display the variation over the entire area at once.

Several features exist that characterize the spatial distribution (Fig. 3.3): 1) the sill is the nominal value of variation beyond which the curve of the variogram reaches a plateau and becomes stable; 2) the range is the nominal value for the

distance “h” beyond which the variation does not increase any further, i.e., when the curve reaches the sill; 3) the hole effect occurs when the variation decreases for higher “h” to increase again, i.e., the curve drops down and goes up again, indicating a recurrent pattern or a periodicity; 4) the nugget value is present when the curve has an initial variation, i.e., originates at a value >0 of the y-axis,

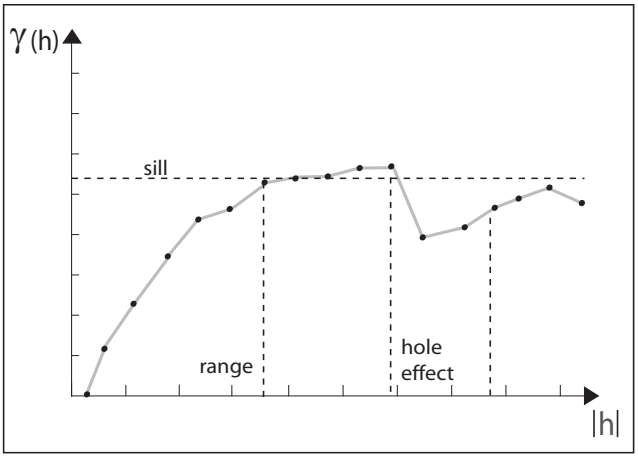

Fig. 3.3: Sample variogram with sill, range, and hole effect

which is due to a random component within the data (e.g., due to a measurement error). None of our fitted variogram models required a nugget.

3.1.1. Other approaches

The better quantification of deformation on a scale spatially smaller than the entire region requires the knowledge of fault displacements. The displacement can be derived from the length of a fault according to a power law that relates displacement and length (e.g., Watterson, 1986; Walsh and Watterson, 1988; Cowie and Scholz, 1992; Davy et al., 1992; Dawers et al., 1993; Scholz et al., 1993; Wojtal, 1994).

However, the exact power law exponent of d-l ratios is still under debate, as it might vary e.g., for extensional and compressional structures, for single faults and those that are interconnected (e.g., Dawers and Anders, 1995; Cartwright et al., 1995; Wojtal, 1996; Cladouhos and Marrett, 1996), for faults in homogeneous or inhomogeneous material (Fossen and Hesthammer, 1997; Gross et al., 1997) etc (cf. Bonnet et al., 2001 for a thorough review). The resulting uncertainty in displacement estimates leaves a range of values that is too big to be used. This uncertainty is even higher when the available digitized geological maps are not very accurate.

3.2. Analogue modelling technique, advantages and limits

In analogue experiments every parameter can be studied separately and in combination, and can directly be related to its effect on the resulting pattern of strain accumulation. All experiments were monitored with a special camera system using the “particle imaging velocimetry” technique (PIV), which allows high resolution of the complete particle displacement fields of strain in time and space. Thus, the effect of every parameter can be studied in detail on e.g., the orogen scale and the next smaller regional scale.

The cameras are to be calibrated before each experimental run. This is particularly important when two cameras are in stereoscopic view for 3D resolution. The calibration yields a mapping function accounting for any distortion, and was applied to the recorded sequential pairs of stereoscopic images. For 3D experiments, digital elevation models were additionally calculated for every stereo image pair by cross-correlation, which were further used for the calculation of the vector fields.

A special algorithm employing Fast Fourier Transformation was executed with the commercial software DaVis by LaVision. Thus, the complete particle displacement field with all components of the strain gradient tensor is resolved with an accuracy of 0.33 mm (viscous-brittle experiments) and 0.38 mm (granular experiments) for every pixel. The pixel error is one order of magnitude lower than its resolution, which is below the scale of a single grain of sand (~400µm). For the granular series, images were sampled every second, rendering 24 images per centimeter of convergence at a motor speed of 2.5 cm/min. For the brittle-viscous experiments, image pairs were taken every five minutes, i.e., every 0.6 mm of shortening at a motor speed of 7 mm/h.

The pixel resolution is limited by the size of the recorded area. A bigger experimental surface requires the cameras to be at a larger distance, thus reducing the resolution. This constraint precludes the high resolution of structures below the fault-scale (e.g., stick-slip behaviour of single grains of sand), when the orogen-scale is to be recorded at the same time. Therefore it can be said that the changes in the velocity fields suggesting deformational stages (cf. Chapter 8) are real and not due to the stick-slip behaviour of grains. However, materials need to have a high elastic

component and to be velocity-strengthening for real analogue earthquakes to occur (Rosenau et al., 2006); also, the normal load has to be higher. Further, the temporal resolution (in the viscous-brittle experiments) has to be much higher to record this instantaneous motion, which occurs within seconds.

All granular materials used in our experiments were tested in a ring shear device. Shear stresses were measured for known applied normal loads. Regression analysis then was used to determine the coefficients of friction and cohesion (according to the Coulomb failure criterion: $\tau = c + \mu \sigma$) for peak, static-stable, and dynamic-stable frictions (e.g., Lohrmann et al., 2003; Hampel et al., 2004), which correspond to the frictional strength until failure, the strength of fault reactivation, and the strength of actively deforming material (Byerlee, 1978). The rheological properties of the viscous mixtures were measured with a TA Instruments AR1000 rheometer under applied shear rates on the order of 10^{-5} s^{-1}.

The viscosities had power law relations with exponents close to 1, classifying them as quasi-Newtonian materials. They are not sensitive to changes in convergence rate, i.e., motor speed. Only non-Newtonian materials show time-dependence, so we created different time scales artificially by leaving out some of the recorded time steps.

All experiments are dynamically scaled. The scaling procedures are described in detail in Chapter 6 (granular series) and Chapter 7 (viscous-brittle series). This allows the comparison of strain evolution in the models to that in the natural example. As we are interested in the general nature of deformation processes, the exact geometric and kinematic similarity and the precise deformation activity over time of single faults is not aimed for.

On these lines, the reproducibility of experiments does not require a precise one-to-one, i.e., the same structures do not need to have exactly the same position with identical geometries and the same timing of strain localization and duration of deformation activity. Instead, the strain pattern, the general strain evolution and resulting deformational system had to be reproducible, including the same aspect ratios.

The cross-shaped pattern (Fig. 7.5, 7.8, cf. Chapter 7 for details) in some of my vise experiments is the same as in some experiments from Cruden et al. (2006), even though the initial model set-up is not the same: experiments by Cruden et al. (2006) allow lateral extrusion, which was not possible in our vise set-up. Similarly, the pattern shape of experiments by Cagnard et al. (2006) resembles the plateau-initiation settings (Fig. 7.5, 7.8, cf. Chapter 7 for details), even though strain localization is initiated in the center of their set-up by a velocity discontinuity.

The preparation of the viscous-brittle experiments set-up requires a special technique. When the the viscosity contrast of the lithosphere (upper crust, lower crust, and mantle lithosphere) and the asthenospheric mantle is low, the asthenosphere affects deformation of the lithosphere. To minimize this effect, the viscosity of the asthenosphere was chosen to be very low. Low-viscosity silicone is an expensive option; water is a good alternative, as long as all layers above have densities below 1.

However, it is not easy to place the viscous layers in the tank without spilling water on top, in which case the layers would immediately sink down. Freezing the water together with the plexiglass tank is not an option as the screws in the plexiglass tank are not made for temperatures of –60°C (the temperature of the freezer was not to decrease). Instead, the layers were frozen themselves.

Therefore, all layers are allowed to float into contact as one big block comprising all viscous parts of the experiment and are frozen thereafter. Such a frozen block can easily be put on the water in the tank. Water, accidentally spilled on the viscous block, will freeze instantaneously without imprinting on the viscous layers. When the viscous block has reached ambient room temperature and is fully settled, the brittle upper crust with a mixture of sand and ceramic beads (Z-lights) is sieved on top.

The calibration of the PIV cameras has to be carried out before the model is fully set up. This means that none of the camera appliance (including the carrying poll and the camera cables) must be touched at any instant after the calibration has been finished. Otherwise the calibration has to be redone.

In total, ten vise experiments were carried out, all but one documented in Chapter 7 (cf. Appendix B). For the granular series, more experiments were performed than are described in Chapter 6. They are documented in Appendix B.